Accepted Manuscript

Please cite this article as: Gui K, Ge J, Ye L, Huang L, The piezoelectric road status sensor using the frequency scanning method and machine-learning algorithms, *Sensors and amp; Actuators: A. Physical* (2018), https://doi.org/10.1016/j.sna.2018.12.048

The piezoelectric road status sensor using the frequency scanning method and machine-learning algorithms

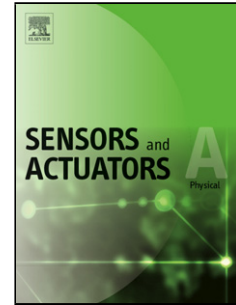Kang Gui[a], Junfeng Ge[a,b,c,*], Lin Ye[a], Lizhen Huang[d]

[a] *Department of Automation, Huazhong University of Science and Technology, Wuhan, Hubei 430074, China*
[b] *National Key Laboratory of Science and Technology on Multispectral Information Processing, Huazhong University of Science and Technology, Wuhan, Hubei 430074, China*
[c] *Department of Computer Science, Norwegian University of Science and Technology, Teknologivegen 22, 2815 Gjøvik, Norway*
[d] *Department of Manufacturing and Civil Engineering, Norwegian University of Science and Technology, Teknologivegen 22, 2815 Gjøvik, Norway*

Research highlights
- Amplitude frequency response was calculated through theoretical model and finite element analysis.
- Nine features were assessed, four calculating methods, including SVR and ANN, were compared.
- The measurement upper limit was extended from 1.4mm to 10mm with accuracy better than 1mm.
- The reproducibility was experimentally investigated and a field test was conducted to proof the sensor.

Abstract
This paper introduces a piezoelectric sensor for measuring the thickness of ice and water film on road surfaces, utilizing the frequency scanning method and machine-learning algorithms. With a constant elasticity alloy plate and a three-electrode piezoelectric transducer disc, this sensor detects ice and water by vibrating. During the research, a model of elastic thin plate with small deflections was built to describe the sensor's vibration characteristics and the sensing unit's amplitude frequency response curves of different ice and water film thickness were recorded. The curves show a high correlation between the thickness of loads and the curve shapes. In order to expand the measurement range, 425 sets featuring vectors for the machine-learning model were extracted, and some specific features such as median, variance, area, centroid and energy under the curves were utilized. The performance of conventional methods and two regression models based on support vector regression (SVR) and an artificial neural network (ANN) were evaluated with cross-validation results. The measurement range of the sensor turned out to be 0 - 10mm. Based on the ANN model, on an average 85.5% and 100% of the neural network outputs had a regression error less than 0.5mm and 1.0mm respectively. Finally, the result of an 18-day field test on the roads of the Norwegian University of Science and Technology is presented.

Keywords: **Artificial neural network, ice detection, piezoelectric sensor, road surface status**

I. INTRODUCTION

ICE formation on certain surfaces can cause serious damage and significant loss. For example, one or two millimeters black ice on the highway is extremely difficult to notice and leads to fatal traffic accidents, costing lives every year. Meanwhile, thousands of tons of de-icing salt and large amounts of manpower resources from road maintenance departments are consumed each time ice and snowy weather conditions appear [1], and the de-icing work causes a lot of waste and environmental pollution for rough road status information and salt usage plans. Nowadays, intelligent transportation system aims to gather as much useful information as possible to help drivers and even unmanned vehicles drive safely and wisely [2]. Under such circumstances, due to the increasingly high requirements of safety and intelligence, detection of road surface status, especially icing conditions has increased in importance. Timely information about icing conditions can help road maintenance departments to design the optimized de-icing plan and thus conserve a lot of salt and manpower from the de-icing work [3]. Accurate road status information can also make unmanned vehicles more intelligent and save lives through a warning on a highway caution plate [4].

Ice sensors have been developed based on different kinds of physical principles, e.g., infrared or laser imaging [5]-[7], fiber optics [8], [9], resonance frequency [10]-[12], ultrasound [13], [14], conductivity [15], [16], capacitance effects [17], [18] and electromagnetic waves [19], [20]. These sensors are applied to meet specific needs in different fields. However, to meet further demands for roads, there are some problems. Road status sensors have been one of the most important devices on highways due to their indispensable role in preventing accidents caused by ice accumulation and waterlogging. But conventional ice sensors cannot provide reliable information about the existence or thickness of black ice on the roads at a minimal cost, and therefore, failing to fulfil the widespread installation requirements from many road management departments. This is vital because most accidents take place when the ice is too thin to be noticed and the inadequate monitoring range increases the risk of miss-detection, especially on highways [16]. Also, numerous commercially available ice sensors cannot identify or measure a water film, whereas this function is commonly needed in a road status information system.

Currently, the most common road status sensors rely on two general methods. One is the polarized infrared or electromagnetic wave measurement method. Colace, Santoni and Assanto [7] measured diffused and reflected infrared light to classify four distinct road statuses: dry asphalt, wet asphalt and asphalt covered with water and ice respectively. This kind of non-contact detection method utilizes polarization technology and covers a relatively large area, distinguishing dry and icy asphalt with promising results. Viikari and his colleagues [20] tested 24-GHz automotive radar to detect road status. The radar worked properly and the method has proven to be feasible. Both Colace's and Viikari's experiments were based on non-contact methods, and a non-contact detection method cannot measure thick ice or water films, which makes it very hard for the sensor to evaluate the severity of the road status. Meanwhile, almost all non-contact detectors are sensitive to the incident angle and installation height, which leads to field regulating problems. Situations on the road are quite complicated, and if black ice is covered by snow, the non-contact detector will be unable to recognize the icy road status. Furthermore, non-contact detectors are more likely to be affected by foggy or rainy weather. Also, and the price of commercial products is very high at present.

The other method is the embedded measurement method. Troiano *et al.* [18] made a low-cost flush-mounted capacitance sensor to detect ice and water on the roads. It is driven at different frequencies and is able to characterize icy, wet and dry statuses reliably. Nevertheless, the capacitance is unstable and thus the sensor cannot tell the thickness of ice or water film. Salt has been widely used to deice on the road. This kind of sensor is affected by the salinity of the water and ice. Du *et al.* [15] implemented a pole style conductivity measurement sensor array. The principle is suitable for road status recognition, but still has the same problem as the capacitance sensor dose. Zou, Ye, and Ge [9] developed a compound fiber optic sensor for ice detection, and this sensor is effective in the measurement of film thickness, especially in identification of ice type. However, the fiber is too weak to be installed on the surface of the road and this sensor is currently unable to distinguish between ice and water. Zhao and Rose [13] proposed an ultrasonic-based ice detector that can locate ice film on a dry thin metal plate by setting a piezoceramic array around the area to be monitored. This technology may be very useful on an airfoil and jet engine, but is not suitable for road status monitoring. Microwave technology has also been used in the embedded measurement method by road status sensor manufacturers. The main function of this kind of sensor is to measure the thickness of water film as well as ice or snow film lying on the road. The readings are reasonably accurate, but this kind of sensor cannot distinguish the loads very well.

All of the above sensors perform well in certain fields, but are not functional enough for road status detection, especially for the measurement of black ice. Consequently, a new method needs to be developed to monitor road status in the case of black ice. Roy *et al.* [11] made an ice detection system based on a metallic plate and a piezoelectric transducer (PZT), but the measurement range is about 0 - 0.5mm, which is too small for a road sensor. Based on Roy's idea, Li *et al.* [10] proposed an ice sensor made of a brass plate and a piezoceramic disc. Theoretical calculations agree with the experimental results of their research, but the sensor's sensing unit is large and thin (with the diameter of 45mm and thickness of 0.127mm), which can be easily damaged by tires. And the measurement range for ice film is about 0 - 1.4mm. Thus, this range is enough for black ice detection, but still too narrow for most of the icing conditions.

Roy's and Li's idea is inspiring and this piezoelectric structure is quite suitable for water and black ice measurement. However, they used the resonance frequency of the sensing unit to measure the ice. To be more specific, the first order resonance frequency of the sensor was utilized to calculate the thickness. This method seriously restricts the measurement range of the sensor. Because of ice accretion, the damping of the vibration system grows rapidly and the amplitude of peak decreases. This leads to the failure of detecting the resonance frequency and to instability of the readings. Consequently, a more feasible method, such as SVR or ANN should be applied to enlarge the measurement range and improve the stability of the sensor.

Moreover, to apply this kind of sensor on the road, some improvements have to be made. First of all, the structure should be tough enough so that tires will not do any harm to the sensor. In this case, the metallic plate should be thicker and smaller, reducing the risk of being bent. Secondly, the measurement range must be extended to meet the needs of road sensors. This can be accomplished by analyzing the amplitude frequency response curves and applying machine-learning models. Thirdly, Roy and Li did not fix the temperature drift of the sensor. Temperature in the road ranges from about 50℃ to -30℃ and common metal suffers a large temperature coefficient. In this case, proper materials must be selected to make the sensor, and temperature compensation should be considered. Lastly, Li analyzed the basic principle of the resonance sensor and manually measured the resonance frequency in the lab with a function generator and oscilloscope. Without a compact and reliable printed circuit board (PCB) and a proper frequency scanning method, the readings will suffer errors from manual operation and the sensor can never be applied on roads.

This paper proposes a road status sensor using a constant elasticity alloy and resonant piezoelectric transducers. The sensor is based on the frequency scanning method, and on account of the embedded algorithm, it is capable of measuring up to 10mm ice or water film with an accuracy of 0.5mm. The paper illustrates the design and experimental issues that appeared in its development. First, the basic physical principle of the sensor is shown. Secondly, according to this theory, a finite element analysis is done to simulate the resonant modes of the vibration system. On the basis of model analysis, road status sensors with frequency scanning circuits are designed and implemented. Experiments are then conducted to measure the temperature drift of the sensing unit and to calibrate the sensor. Conventional fitting curve methods and two different machine-learning models are assessed based on the features extracted from the experimental data. In addition, the application test of the road status sensor at the Norwegian University of Science and Technology is briefly introduced. The field test lasted for eighteen days, and the sensor worked properly during the

II. Sensor design

The sensor measures ice film thickness and water film thickness using the amplitude frequency response curves of the sensing unit. Thus, it is important to figure out the response characteristics when designing the sensor. Consider an alloy plate bonded with a piezoceramic disc, as is shown in Fig. 1. Add the load, e.g., the ice film or water film, on the upper surface of the plate, and then drive the piezoceramic disc with sinusoidal voltage of different frequencies. A vibration system is thus formed. In general, the whole vibration system could be considered as a thin elastic plate with small deflections. In this case, the natural angular frequency and amplitude frequency response curves can be numerically solved by establishing a proper mathematical model. Detailed formula derivation processes and calculation methods are described in the appendix.
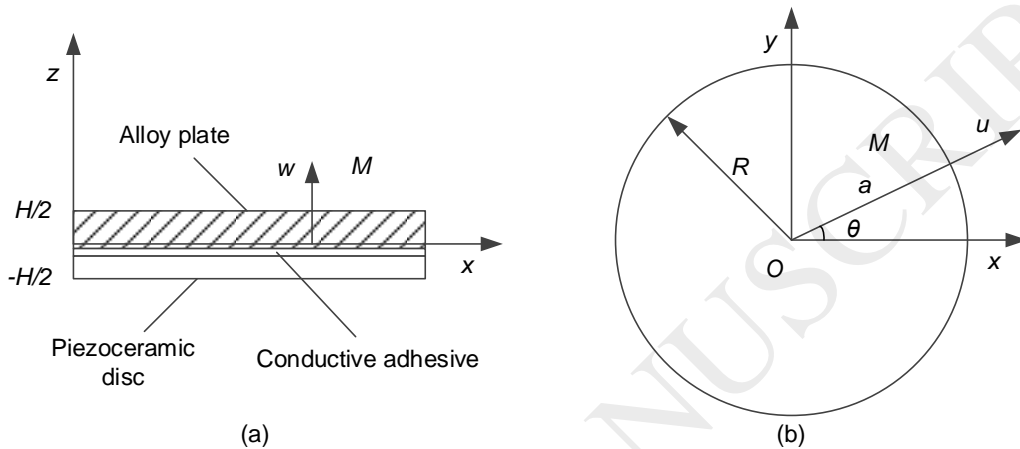

(a)   (b)

Fig. 1. A schematic view of the sensing unit of road status sensor, and water or ice film lies on the upper surface of alloy plate. (a) is the side view in Cartesian coordinates and (b) is the top view in polar coordinates.
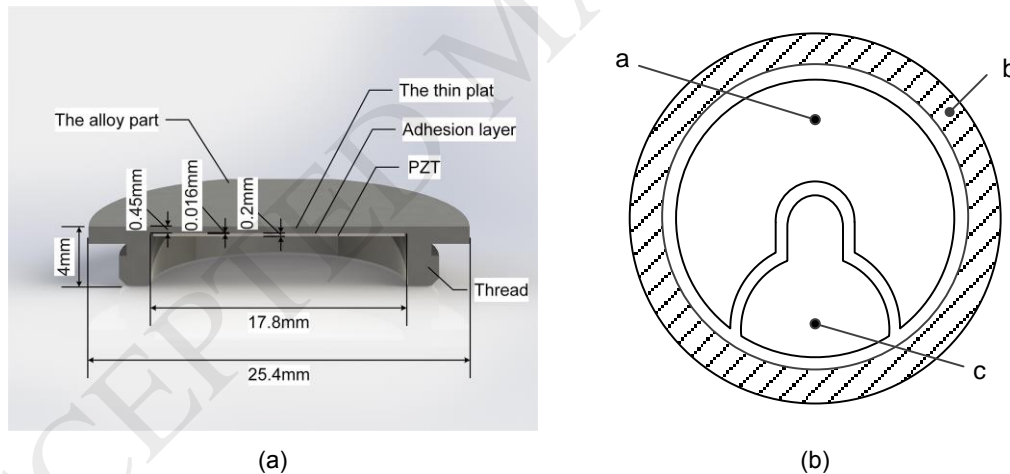

(a)   (b)

Fig. 2. A schematic view of the sensing unit of road status sensor. Water or ice film lies on the upper surface of alloy plate. (a) is the cross section view of the sensing unit and (b) is the bottom view, three electrodes are set on the surfaces of the sensing unit separately.

Two parts are included in the appendix. Appendix A describes the frequency feature of an elastic thin plate with small deflections, and appendix B builds an equivalent bending modulus model to calculate the numerical solution of the vibration system. This model is more accurate than Roy's and Li's models due to the derivation of the natural angular frequency formula and consideration of Poisson's ratio in the bending modulus model in appendix A. At this point, the natural angular frequency ω_n and the amplitude frequency response $A(\omega)$ of the equivalent bending modulus model can be calculated from the physical parameters of materials. It can be derived from Eq. (A.8) and Eq. (B.5) that ω_n will increase with the growing of ice film and decrease with the accretion of water film, as Young's modulus of water is considered as 0. Furthermore, Eq. (A.10) and Eq. (B.5) indicate the change of the amplitude frequency response curve. With the growing of ice film, the peak of the curve will shift to a higher frequency and the amplitude will decrease on account of the rising damping. On the other hand, with the accretion of water film, the peak of the curve will shift to a lower frequency and the amplitude will barely change. As for the ice under snow situation, theoretically, the dry snow won't affect the measurement of the piezoelectric sensor. The structure of snow is very loose and porous, the density is about 5% to 10% of water. Hence, the mass enhancement caused by it can be ignored in most of conditions. Moreover, the snow doesn't

affect the equivalent bending modulus of the vibration system, therefore the sensor is immune to a few millimeters dry snow.

To utilize the vibration characteristics of the equivalent bending modulus model described in the appendix, a multilayer structure has been designed, as is shown in Fig. 2. The structure is the main part of piezoelectric sensor. In this structure, a piezoceramic disc is bonded with an alloy part using conductive adhesive. The alloy part is a thin plat surrounded by a screw thread structure, the diameter of the thin plat is 17.8mm and the diameter of the whole alloy part is 25.4mm. The sensing unit is embedded in the heavy stainless steel shell with thread and conductive adhesive. The depth of the thread is 3mm, and the shear strength of the adhesion is about 8MPa/cm2, therefore the connection between the sensing unit and the steel shell is very strong. In this way, the sensing unit is firmly fixed in the road status sensor and the displacement of the bonding surfaces can be regarded as zero.

The piezoceramic disc has three electrodes 'a', 'b', 'c', which are insulated from each other. Electrode 'b' contains the alloy plate, the conductive adhesive and the top surface of the piezoceramic disc, and is connected to the ground of sensor circuit so that electric current on 'a' and 'c' can each form a loop. Electrode 'a' contains the most area of the piezoceramic disc's bottom surface and is connected to the driving part of the sensor circuit. The inverse piezoelectric effect has been utilized in this part. Sinusoidal voltage of different frequencies is loaded between 'a' and 'b' periodically to cause the structure to vibrate. Electrode 'c' is connected to the sensing part of the circuit. According to the principle of piezoelectric effect, the biggest deformation leads to the highest voltage and the deformation of the center turned out to be the largest, so 'c' occupies the center and the rest area of bottom surface to ensure good feedback voltage.

Table 1 The parameters of constant elasticity alloy, PZT, adhesive, water and ice.

	Young's modulus (GPa)	Density (kg/m^3)	Poisson's ratio	Thickness (mm)	Diameter (mm)
Alloy	206 [a]	8100 [a]	0.33 [a]	0.45	17.8
PZT	50 [a]	7700 [a]	0.30 [a]	0.20	17.8
Adhesive	5 [a]	2520 [a]	0.38 [a]	0.016	17.8
Water	0	1000	0.50	-	-
Ice	9.0	918	0.33	-	-

[a] Provided by the manufacturers

Table 1 lists the materials used in the sensor structure implementation and their main parameters. The dimension parameters indicate the size of vibration part. The parameters of water and ice are also given in the table. In accordance with Eq. (A.8) and Eq. (B.5), the elastic modulus is one of the key parameters that affect the value of ω_n and $A(\omega)$, so the alloy plate is made of a constant elasticity alloy, which has a quite small elastic module temperature coefficient. This design has been imported into finite element simulation software COMSOL Multiphysics 5.3a. Characteristic frequency analysis and mode analysis were solved to figure out the characteristic frequencies and the amplitude frequency response.
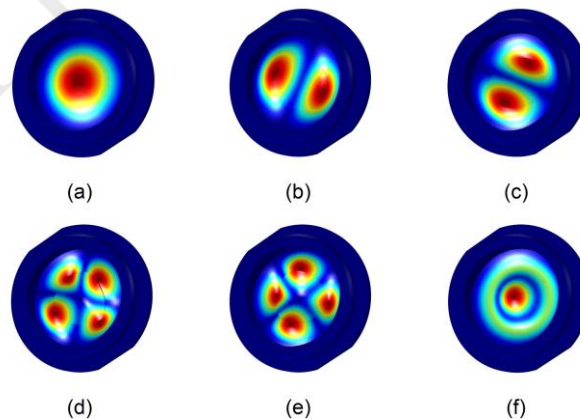

Fig. 3. (a) to (f) are the first six orders of no-load mode shapes respectively. The displacement of dark blue part is zero, and the dark red part represents the maximal displacement region.

The first six orders of no-load mode shapes are given in Fig. 3. The photos suggest that the second to the fifth modes are generally inversely symmetrical at any moment during a complete vibration cycle, so the average displacement of each mode is very close to zero, whereas the first and the sixth order modes are central symmetric and the average displacement of the vibration surface turns out to be much larger. According to the principle of piezoelectric effect, greater average displacement means more electric charges and thus higher piezoelectric voltage. In this case, the first and the sixth order modes are likely to generate much

more electric charge than the other four modes, so the piezoelectric voltages of these two modes should be very high.

The theoretical calculation results and part of the simulation results are described in Fig. 4. The response of the first mode was calculated through Eq. (A.10), the frequency range was limited from 10 kHz to 30 kHz, and the step length was 50Hz. On account of the definition of elastic thin plate with small deflections, the thickness of the vibration system H should be far less than 2/5 of the neutral strain plane's radius R, which has been stated in appendix A, so the thickness of the whole vibration system should be far less than 3.56mm. As a result, the thickness of ice and water films was limited to the 1mm range in the theoretical calculation results, and the damping coefficient was set as 0.01. Finite element analysis has been done in the range of 7 kHz to 200 kHz with a step length of 50Hz. The thicknesses of ice films were from 0mm to 10mm with a minimal step length of 0.2mm and the thicknesses of the water films were from 0mm to 12mm with a minimal step length of 0.2mm.
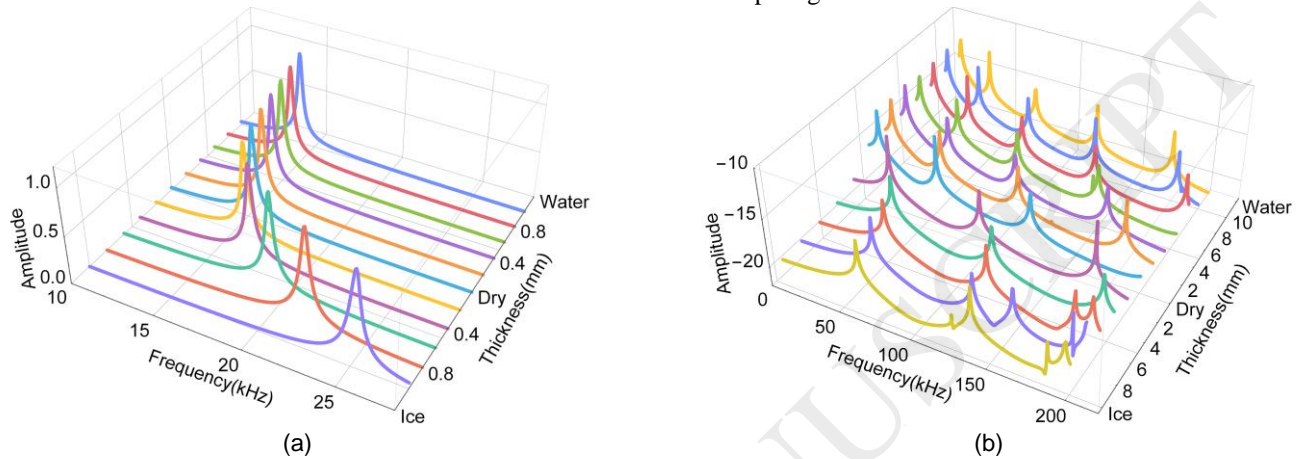

Fig. 4. Theoretical calculation results and part of simulation results of different load statuses. (a) is the normalized amplitude frequency response curve of the first order mode vibration based on theoretical calculation, and (b) is the simulated amplitude frequency response curve in log coordinates from 7 kHz to 200 kHz.

In the theoretical calculation and simulation models, the conductive adhesive film has been ignored due to its low thickness. As a matter of fact, the theoretical calculation results suggest that the first order resonance frequency of dry status will increase only 40Hz, which is 0.26% of the frequency value, if the adhesion layer is not considered. On the other hand, simulation results also prove the adhesion's little impact on the amplitude frequency response. However, finite element analysis platform has to generate very fine standard tetrahedral structure for the thin adhesion layer. And the cross-sectional area of this layer is equal to the other layers. Thus modeling of the adhesion layer will bring catastrophic rise of the element number, which will lead to higher complexity and much longer solving time. A fine standard mesh generation has been employed in this study, it suffers from the thickness of adhesion layer. The number of element rises rapidly, the solving time of one condition increases from 8 hours to more than 60 hours, which is unacceptable since dozens of test conditions are going to be solved. Thus all the calculation results presented in this work were done in a simplified model without adhesion layer.
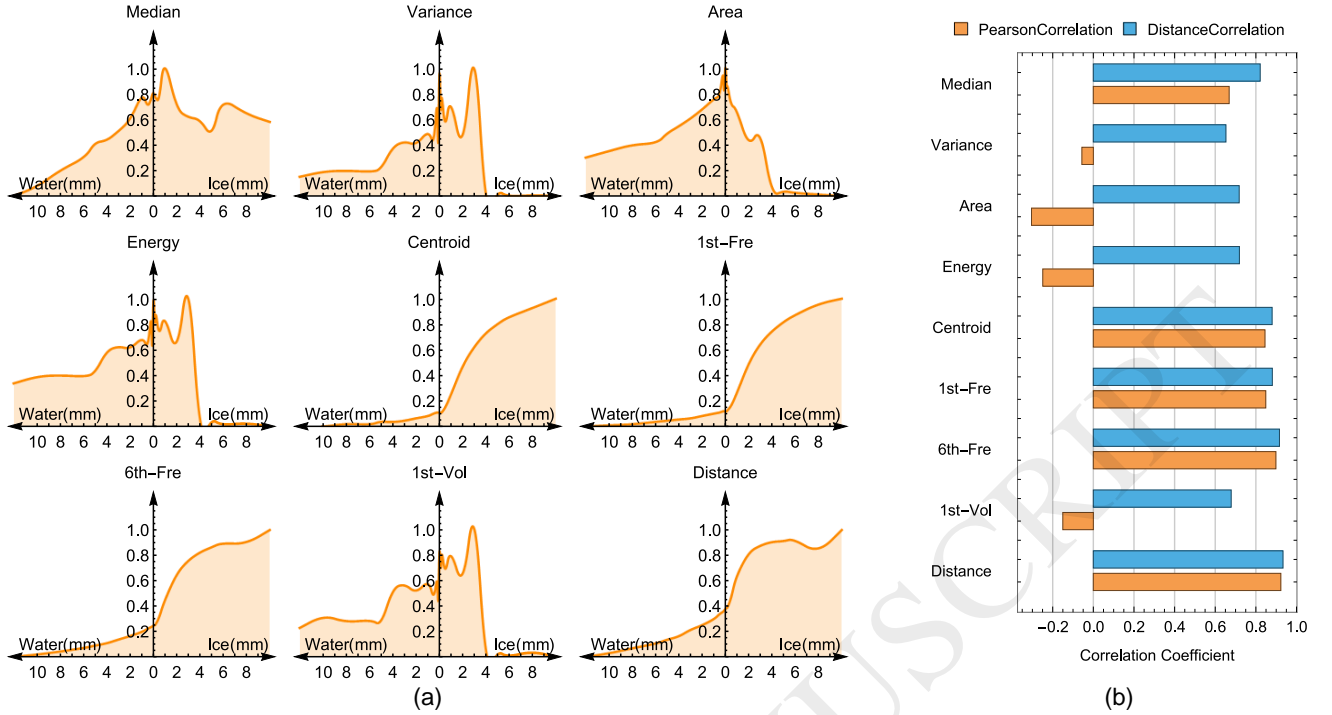
Fig. 5. Features extracted for surface status detection. (a) shows the change of the normalized feature value with growing of ice film and water film thickness. (b) illustrates the Pearson correlation coefficient and distance correlation coefficient of the features.

According to the results, the peaks of the amplitude frequency response curve moved to a lower frequency section with water accretion, and shifted to a higher frequency section with ice growing, in both the theoretical calculation as well as the numerical simulation. The theoretical calculation and the simulation were in agreement with the values of the first order resonance frequency. The maximum error was found at 1mm-thick ice model, and the error was less than 6.9%. In other cases, the absolute error was better than 500Hz, which was less than 3.8% of the resonance frequency. Furthermore, the curves of the two methods matched well at the shapes of the first order resonance peaks. Taken together, the curves suggested that the theoretical calculation and the numerical simulation proved each other on this vibration model.

Under such circumstances, the result of the simulation can be utilized to extract more key features because it contained much more information than the mathematical model built in the appendix. Feature analysis based on simulated data was done to study the feasibility of applying the machine-learning algorithms to the sensor. The features that commonly utilized in waveform analysis were extracted, such as median, variance, area and energy under the curves, centroid, positions of peaks, and distance between peaks. These features are all potentially useful, as is presented in Fig. 5. In total, nine features have been extracted to form the feature vector. All the values were normalized into range of 0 to 1 for easier and better comparison. Each subplot in Fig. 5(a) shows the change of the feature value with the growing of ice film and water film thickness. Apparently, the monotonicity of the feature curves is the most important indicator for surface status detection. Compared with other features, centroid, the first and the sixth order resonance frequencies are the best three features for both ice and water measurement, and the curves are almost perfectly monotonic. In contrast, the area under the amplitude frequency response curve is non-monotonic in the whole measurement range, but it decreases with the thickness of ice film and water film. Thus, it can be used to measure the thickness of the load instead of identifying the surface status. Distance between the peaks is not strictly monotonic when ice film thickness exceeds 6mm, so it can be utilized to measure water and thin ice. Other features such as median, variance, energy and voltage of the first order resonance frequency are less effective due to the fluctuation of the feature curve.

The correlation coefficient of the features is shown in Fig. 5(b). Pearson correlation and distance correlation have been utilized to evaluate the correlation between each individual feature and load thickness. The coefficient calculation between the random variables X_k and Y_k (k=1, 2, …, n) is obtained through (1) and (2), and ρ stands for the Pearson's correlation coefficient:

$$\rho_{X,Y} = \frac{\text{Cov}(X,Y)}{\sigma_X \sigma_Y}, \qquad (1)$$

where Cov is the covariance and σ is the standard deviation of the random variables. dCorr is the distance correlation,

$$\text{dCorr}(X,Y) = \frac{\text{dCov}(X,Y)}{\sqrt{\text{dVar}(X)\text{dVar}(Y)}}, \qquad (2)$$

where dCov is the distance covariance and dVar is the distance standard deviation. The distance standard deviation dVar(X) can be regarded as dCov(X,X), so dCov and dVar in (2) can be solved as

$$\text{dCov}^2(X, Y) = S_1 + S_2 - 2S_3 \, , \qquad (3)$$

where S_1, S_2 and S_3 can be obtained as

$$S_1 = \frac{1}{n^2} \sum_{i=1}^{n} \sum_{j=1}^{n} \lVert X_i - X_j \rVert_{dX} \lVert Y_i - Y_j \rVert_{dY} \, , \qquad (4)$$

$$S_2 = \frac{1}{n^2} \sum_{i=1}^{n} \sum_{j=1}^{n} \lVert X_i - X_j \rVert_{dX} \frac{1}{n^2} \sum_{i=1}^{n} \sum_{j=1}^{n} \lVert Y_i - Y_j \rVert_{dY} \, , \qquad (5)$$

$$S_3 = \frac{1}{n^3} \sum_{i=1}^{n} \sum_{j=1}^{n} \sum_{k}^{n} \lVert X_i - X_k \rVert_{dX} \lVert Y_j - Y_k \rVert_{dY} \, . \qquad (6)$$

Pearson's correlation coefficient has been widely used in research. This coefficient ranges from -1 to 1, and is believed to be more suitable to represent the correlation in linear relationship between feature and label. If the coefficient is close to 0, then there is little linear correlation between the two variables. Meanwhile, if the value is negative, then it is a negative correlation. However, in practice, most of the relationships between feature and label tend to be nonlinear. To overcome the disadvantage of Pearson's correlation coefficient, a distance correlation coefficient has been employed. The bar chart in Fig. 5(b) suggests that variance and the voltage of the first order resonance frequency score the lowest in both the Pearson correlation and in distance correlation. But other seven features are closely related to the surface status, so the feasibility of the new method is proved, and the experiments can proceed with a coarse expectation.

Overall, part of the extracted features are suitable for surface status detection in accordance with the simulation results, but the model used for finite element analysis has been simplified and temperature drift has not yet been considered. Thus, the temperature stability of the features should also be calculated before importing them into the machine-learning model.

III. EXPERIMENT

The mathematical model and simulation results imply that the shape of the amplitude frequency response curve is highly correlated to the load status on the sensor. However, the curves obtained in the experiment would be partially different from the simulation result, due to the simplification of the structure and the parameters. The experimental work focused on the analysis of frequency scanning data obtained by the road status sensor and choosing relevant features. The experiment was conducted in a temperature chamber, and the detailed experimental setup is described in Fig. 6.
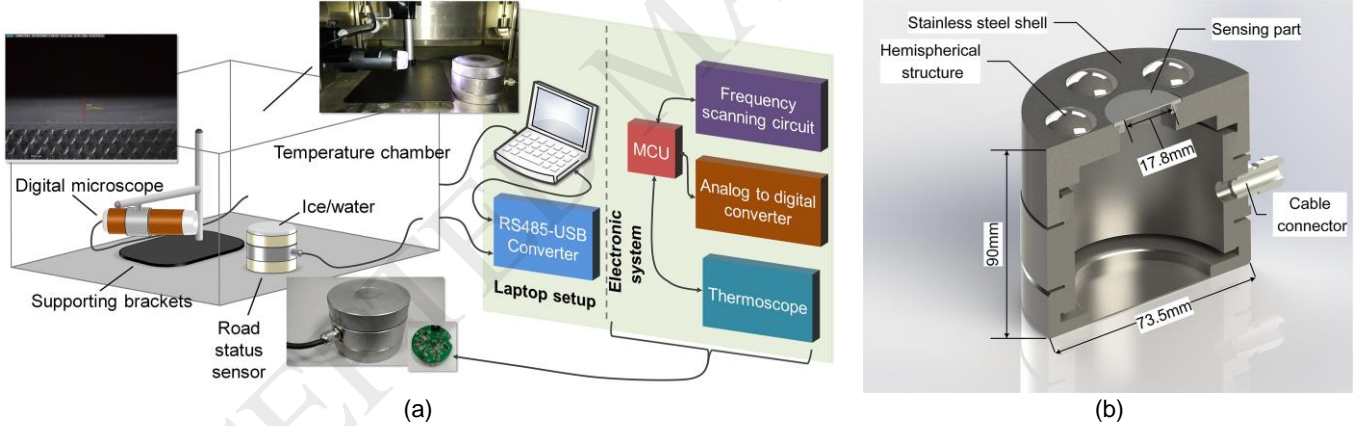

Fig. 6. (a) Experimental setup to collect data of the amplitude frequency response curve of a road status sensor. (b) The cross section schematic of road status sensor, the silicone seals, the cables and the printed circuit board are omitted.

During the experiment, the sensing unit made of the piezoceramic disc and alloy plate was embedded on the top of a stainless steel structure and a printed circuit board was installed inside the steel shell. The road status sensor is 90mm tall with a diameter of 73.5mm, the hemispherical structure is designed for the sensor protection, but not used in the lab test for better view of the microscope. Therefore the sensor is strong enough to be installed in the road.

The electronic system on the circuit board includes a microprogrammed control unit (MCU), a frequency scanning circuit, an analog to digital converter and a thermoscope. Electrodes of the sensing unit were connected to the frequency scanning circuit and the analog to digital converter, and a cable for data transmission and power supply connected the circuit to a RS485-USB converter. The pictures of the road status sensor and the printed circuit board are shown in Fig. 6. Meanwhile, a digital microscope was installed on supporting brackets next to the sensor, and was used for measuring the real thickness of ice film and water film. A picture of the view from the microscope is shown near the schematic diagram. The resolution of the microscope is 0.001mm and the measurement range is more than 20mm. A laptop was set out of the temperature chamber and a video data stream from the digital microscope and frequency scanning data as well as temperature data from road status sensor were transmitted to the laptop.

The frequency scanning circuit and the analog to digital converter were designed to obtain the amplitude frequency response data. Under the control of a MCU, the frequency scanning circuit generated sine waves of the same amplitude and different

frequencies between electrode 'a' and 'b' of the sensing unit. In accordance with inverse piezoelectric effect, the piezoceramic disc drove the sensing unit to vibrate. Then, the mechanical vibration was modulated by the structure of the sensing unit and the sensor load. Meanwhile, the piezoelectric effect converted this mechanical feature into electrical signals between electrodes 'a' and 'c'. Lastly the analog to digital converter measured the voltage between electrodes 'a' and 'c', and delivered the maximum voltage value to MCU under every different frequency. The frequency scanning range was from 7 kHz to 220 kHz with a step length of 50Hz, so every scanning cycle will generate 4260 voltage values. By putting all the voltage data together, the amplitude frequency response curve can be plotted. A thermoscope in the steel shell measured the temperature of the alloy plate at all times.

In order to prove the performance of the road status sensor, three kinds of feature curves have been collected during the experiment, including a temperature drift curve, an ice feature curve and a water feature curve. To begin with, a temperature drift experiment was conducted. The temperature chamber provided a temperature controlled environment ranging from -40℃ to 150 ℃. A road status sensor with dry and clean surface was put into the chamber, and the sensor temperature was monitored by the thermoscope inside the sensor. The chamber temperature was adjusted to change the sensor temperature. And the amplitude frequency response data were collected every 5℃ from 60℃ to -30℃, the temperature was subject to sensor temperature. This experiment aimed to find out the drift of the amplitude frequency response curve with temperature and to prove the stability of the sensor. The temperature drift experiment was repeated five times. Secondly, the chamber temperature was set to -5℃, -15℃ and -25℃ respectively to simulate the situation on most of the highways, and droplets with a diameter of about 100 micrometers from a bucket of ice water mixture were sprayed on the sensor slowly through a pump. When ice grew on the sensor's upper surface, the amplitude frequency response data and the real thickness of ice film were recorded. In this way, the ice feature curve of the sensor was obtained and the ice film thickness ranged from 0.1mm to 10mm. In total, twenty-one sets of data points were collected, and in order to ensure better accuracy of calibration, the experiment was repeated more than five times. Then the chamber temperature was set to 5℃ and 30℃ respectively, and water droplets with a diameter of about 100 micrometers and temperature of 5℃ and 30 ℃ were sprayed on the sensor slowly through a pump. When water accreted on the sensor's upper surface, the amplitude frequency response data and the real thickness of the water film were recorded. The water film thickness ranged from 0.1mm to 12mm, and in total, eleven sets of data points were collected. After repeating the tests five times, the water feature curve of the sensor was calibrated. Finally, a reproducibility test was done to evaluate the accuracy of calibration, and in total, 61 sets of data points were tested.

IV. RESULTS AND DISCUSSION

A. Temperature characteristic study

According to the parameters provided by the manufacturer, the elastic module temperature coefficient of constant elastic alloy is about -1.8×10-5℃-1, and the temperature drift of alloy can be given by the following formula:

$$\beta \cdot E = \frac{dE}{dT},\qquad(7)$$

where β stands for the elastic module temperature coefficient of constant elastic alloy, E stands for the elastic module of alloy, and T stands for the temperature of alloy. In this case, when the temperature drifts 90℃, the elastic module would only drift about 3.3×10^8Pa, which is about 0.16% of the alloy's Young's modulus. The temperature drift experiment has been conducted five times, and the consistency of the data is perfect. The standard deviation turns out to be less than 0.2% of the raw data, which is so small that the impact on measurement is negligible. Thus, an average value has been applied to process the datasets from the experiment and the error bar is omitted. The result of the temperature drift experiment describes the road status sensor's temperature characteristics, ranging from 60℃ to -30℃. The curves drifted a little in the whole temperature range and the drift turned out to be monotonic. As is shown in Fig. 7(a), two typical curves of 60℃ and -30℃ are plotted, and the light pink and light green areas indicate the differences between the two curves. The curve shape is different from the simulation result, but the resonance peaks match well. The differences can be caused by the non-ideal boundary constraint, circuit level signal distortion, and other details ignored in the simulation. During the experiment, the curve shape changed slightly and regularly with the decline of temperature. Taken as a whole, the curve shifted to a higher frequency when the temperature dropped, and the amplitude decreased remarkably in the frequency range from 70 kHz to 140 kHz.

Apparently, the drift also affected some of the features extracted from the curves, as is shown in Fig. 7(b). There are nine features in the figure, including the median and variance of the collected voltage, the area and energy under the curve, the centroid of the curve, the voltage of the first order resonance peak, the first and the sixth order resonance frequency, and the distance between them. The height of the bars in the figure is calculated from dividing the feature value under 60℃ or -30℃ by the feature value under 15℃, so the closer bar height is to 1.0, the better the feature thermal stability. The bar chart suggests that the first and the sixth order resonance frequency, and the distance between them have excellent thermal stability, whereas area, variance and voltage of the first

order resonance peak have bad thermal stability. Moreover, the three features related to resonance frequency turn out to have negative temperature coefficient and the variance has a variable temperature coefficient. In fact, the temperature drift curve of variance is convex, so the further the temperature is from the curve vertex, the bigger variance. The other four features have a positive temperature coefficient.
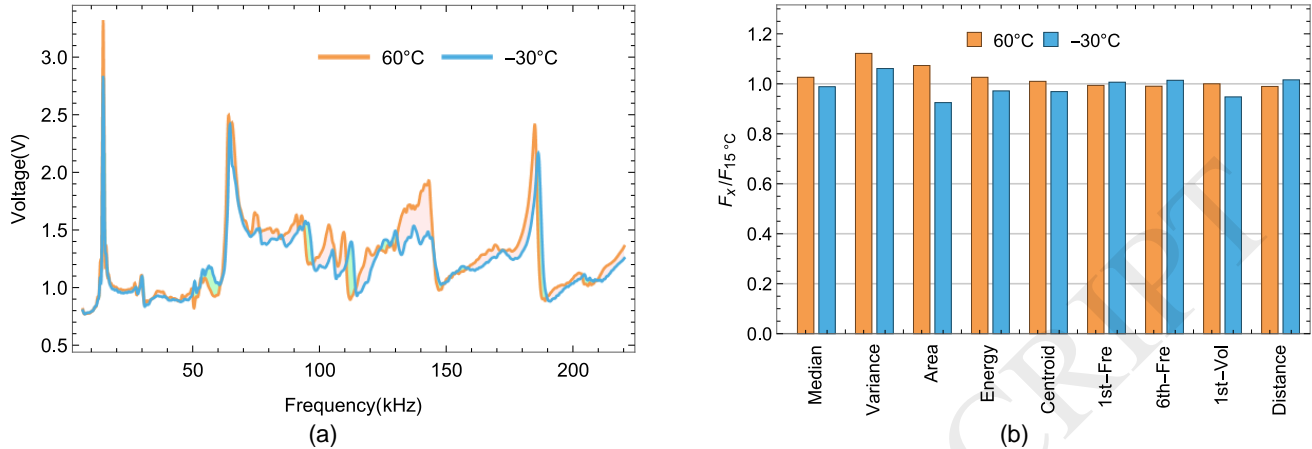

Fig. 7. The result of temperature drift experiment. (a) shows the temperature drift of amplitude frequency response curves of 60℃ and -30℃, and (b) describes the temperature characteristic of nine selected features.

The temperature characteristics of features turn out to agree with the amplitude frequency response analysis in the appendix and (7). The frequency related features drift with the elastic module E and E has a small and negative temperature coefficient, so the first and the sixth order resonance frequency, as well as the distance between them increased slightly with the decrease in temperature. However, other features, such as area, energy, centroid and voltage are more connected to the amplitude of sensor vibration. According to Fig. 7(a), the amplitude decreased with the drop in temperature, and in a certain frequency range, this phenomenon is obvious. Since some modes of sensor vibration will seriously decay as the boundary condition changes, so cold shrinkage might have changed the boundary condition while the drop in temperature brought down the amplitude of mode, and then eventually led to a positive temperature coefficient of the features.

Thus, the sensor itself suffers temperature drift from some aspects, but if the three features with bad thermal stability are removed from the model, the remaining six features only drift less than 4% in the whole temperature range. On the other hand, parameters of ice and water will also drift with temperature. According to the appendix, only the bending modulus D of the vibration system will drift much with temperature and affect the shape of amplitude frequency response curve. Meanwhile, Young's modulus of water is considered as 0, so the drift of water can be ignored. However, Young's modulus of ice shifts with temperature and the freezing time, thus temperature compensation should be considered in the machine-learning model when measuring load thickness.

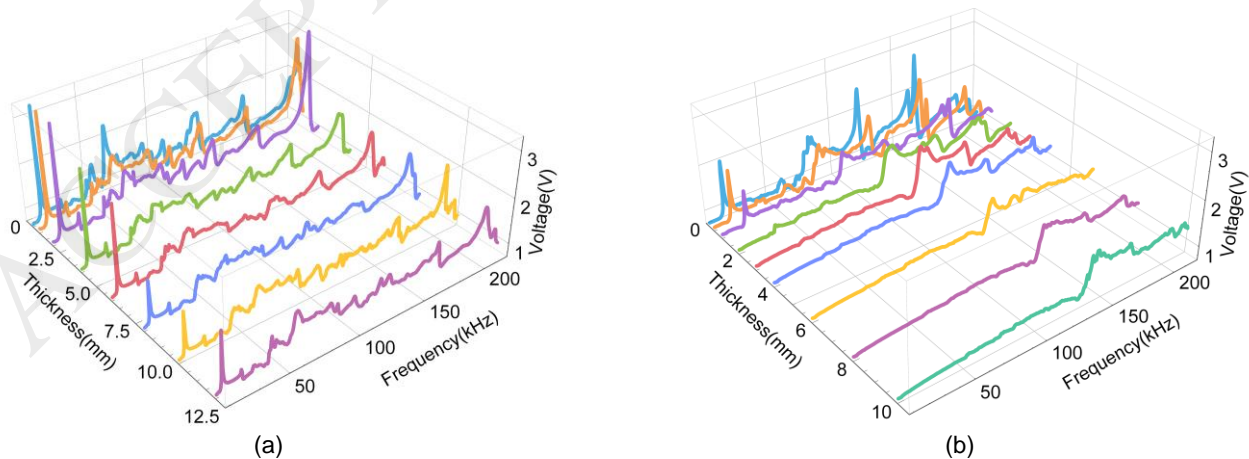*B. Road status recognition and load thickness measurement*

Fig. 8. The results of ice and water film thickness measurement experiment. (a) shows the amplitude frequency response curves of water film thickness measurement experiment under 5℃, and (b) shows the amplitude frequency response curves of ice film thickness measurement experiment under -15℃.
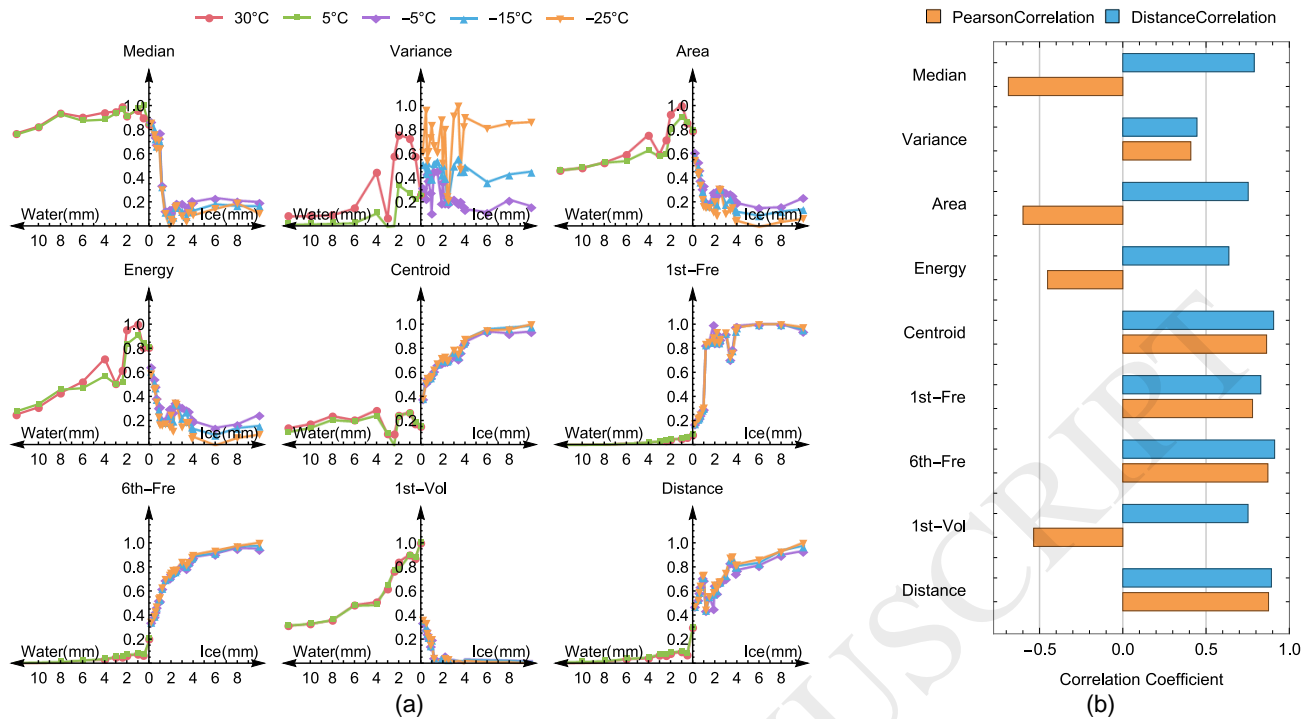
Fig. 9. Features extracted from the results of ice and water film thickness measurement experiment. (a) shows the change of the normalized feature value with growing of ice film and water film thickness, mean values have been used to represent the data of the five times of measurement experiment. (b) illustrates the Pearson correlation coefficient and distance correlation coefficient of the features.

The results of the load thickness measurement experiment have been partly shown in Fig. 8. Water film thickness measuring curves of 5°C are in Fig. 8(a), and only eight curves have been displayed for a clearer view. Ice film thickness measuring curves of -15°C are in Fig. 8(b), and only nine curves have been displayed. Apparently, the shape of the curves is different from the result of simulation due to the simplified model, but the key features of the curves seem to match. The peaks of the curves moved to the lower frequency section with water accretion and to the higher frequency section with ice growing. In the meantime, the voltage of the peaks decreases when load thickness increases, especially for the measurement of ice film thickness. The absolute values of the first and the sixth order resonance frequency extracted from the experimental curves match well with the simulation curves, and the maximum error is better than 10%. All the nine features have been extracted as are shown in Fig. 9. Since the experiment has been conducted five times, the deviation caused by manual operation is unavoidable. For instance, the ice film shape and thickness could not be exactly the same each time water froze during the repeatability tests, and thickness error of less than 0.05mm is acceptable. As a result, mean values have been utilized to represent the data, assuming the error could be reduced by taking the average. Each subplot in Fig. 9 shows five curves of one particular feature. Three are ice feature curves and the other two are water feature curves. The experimental features are extracted in Cartesian coordinates, whereas the simulated features are extracted in log coordinates. Therefore, the values of features may be different but the shape of curves should be similar.

As is shown in Fig. 9(a), a total of thirty-two sets of data points have been plotted. Each set of data points includes fifteen or ten sets of feature vectors due to five repeats of the test and 3 or 2 different temperature groups. Altogether, 425 sets of feature vectors have been processed in this phase, and every feature vector was extracted from 4260 voltage values. The temperature characteristic of all the features agree with the temperature drift bars in Fig. 7(b). Curve shapes of some features such as area, and the first and the sixth order resonance frequency match well with the simulation results. Area suffers from temperature drift and is monotonic with load thickness to a certain extent. The first and the sixth order resonance frequencies have excellent temperature stability and good monotonicity, but there are some fluctuations in the curve, which will affect the calibration accuracy. The curves become flat when load thickness reaches 4mm or more, so it can be inferred that if the first or sixth order resonance frequency of the sensor was used as the only argument to calculate the thickness, the reading would be very unstable and inaccurate. In fact, the glitches in the first order resonance frequency curves are caused by the raising damping and failure of locating resonance peak. To overcome this disadvantage, more features are needed when measuring the thickness of ice and water films.

Consequently, the simulation results and the experimental results all suggest that machine-learning models should be applied to gather more information from the raw data and enhance the stability of the sensor reading. In the meantime, the thickness of load has been limited to 10mm for training and testing the models. Moreover, median and variance are very different from the simulated curves in Fig. 5(a). Variance is almost random in some part of the curves, and according to the correlation coefficient in Fig. 9(b), it only scores 0.445, which is the lowest among all the features. Curves of the other four features are similar with the simulation results, and they should be helpful in the training model to reduce the error caused by the fluctuations of resonance frequency

curves. These features score at least 0.637, which are high enough to be reserved. Thus variance should be removed from the feature vector, and this conclusion is also supported by the simulated feature analysis in Fig 5. The consistency of the simulation results and the experimental results proves the effectiveness of this study. Furthermore, temperature data should be in the feature vector to act as a method of temperature compensation and improve the accuracy.

The conventional method of recognizing the surface status and calculating the load thickness is to fit a curve with the first order resonance frequency and the corresponding thickness data [10], [11]. Nevertheless, according to the feature curves in Fig. 5 and Fig. 9, the first order resonance frequency is not the best choice for this curve-fitting method, and the sixth order resonance frequency turns out to be more stable and monotonic. Table 2 shows the fitting functions obtained through the least square method. The 425 sets of feature vectors extracted in Fig. 9 have been used, and ice and water status are separated for great difference between curve shapes. R-Squared values are listed in the table to indicate the degree of fitting and the dry condition frequency band acts as a barrier to divide the ice and water frequency range.

Table 2 Fitting functions and R-Squared values of the first and the sixth order resonance frequency

Order	Status	Fitting Function (kHz)	R-Squared
First	Ice	$0.000742529x^3-0.0817395x^2+2.91395x-31.7878$	0.590629
	Water	$0.529305x^3-22.3007x^2+313.529x-1472.06$	0.969797
	Dry	$14.45 < x < 17.25$	-
Sixth	Ice	$0.000105586x^3-0.0268625x^2+2.2839x-63.8117$	0.968183
	Water	$0.00708281x^3-0.881034x^2+36.2866x-496.327$	0.975213
	Dry	$46.35 < x < 52.35$	-

The dry condition frequency band is determined by the resonance frequency of real dry data values, and has been expanded to a frequency range of several thousand Hertz for better stability of status recognition. Resonance frequency higher than the upper limit of the dry condition frequency band will be considered as ice status, and frequency under the lower limit will be recognized as water status. The R-Squared values suggest that the ice fitting curve of the first order resonance frequency is hard to represent and the relationship between frequency and ice thickness, which has been deduced during the feature extraction phase. Meanwhile, the sixth order resonance frequency performs much better and the validation as well as test results are shown in Fig. 10. Sixty- one sets of data points have been tested after fitting the curves, and each set of data points includes one set of feature vectors, the load thickness ranges from 0.1mm to 10mm and the temperature ranges from -30℃ to 40℃. The fitting curve method has been markedly improved by utilizing the sixth order resonance frequency according to the error distribution plots in Fig. 10(a) and (b). The error values are significantly decreased in a much larger measurement range compared with conventional sensors. In the meantime, the validation error distribution is similar with that of the test error, which guarantees the generalization ability of the fitting curves. However, the error of thin ice is too large for black ice detection, and the error of thick load keeps increasing, so there is still room for improvement.
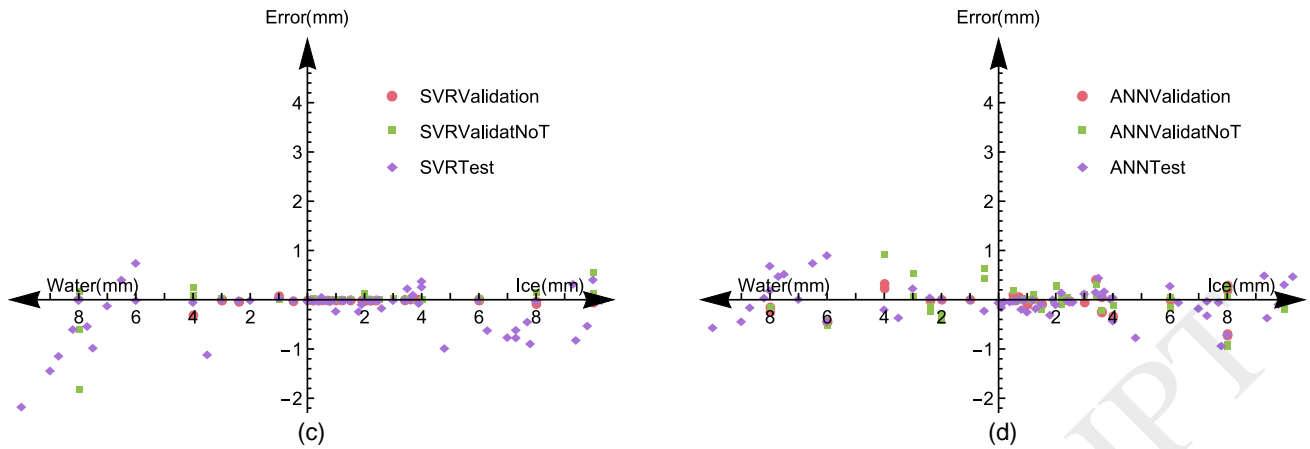

(a)

(b)
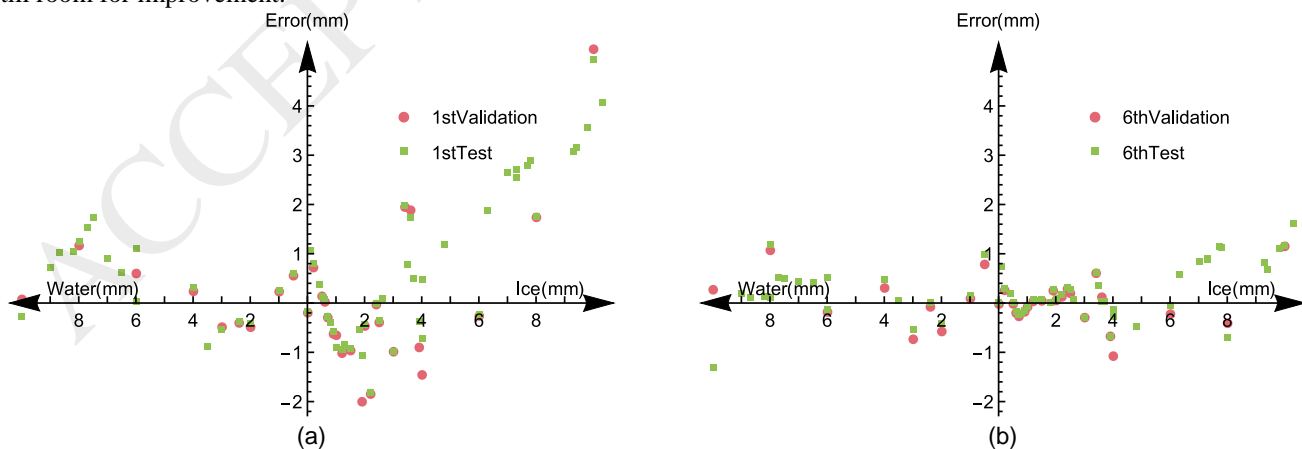
Fig. 10. Error distribution of fitting curve methods, the SVR and the ANN models. (a) is error distribution of the first order resonance frequency fitting curve, (b) is error distribution of the sixth order resonance frequency fitting curve. (c) is error distribution of support vector regression model and (d) is error distribution of artificial neural network model. "ValidatNoT" in the legend stands for the validation data of the training model without temperature compensation.

To achieve more accurate and stable measurement, two models including SVR and ANN have been adapted, using the 425 sets of feature vectors. In the model settings, 80% of the feature vectors have been added to the train set and another 20% have been filled in the validation set. The vectors are all randomly selected. The SVR model uses the Gaussian kernel function with gamma value searching in the range of 4 to 10 with a step length of 0.01 and the punishment coefficient for loss function is searched in the range of -10 to 10 with a step length of 0.1. The ANN model is constructed with an input layer, two hidden layers and an output layer. The hyperbolic tangent sigmoid transfer function is chosen in the hidden layers and the output layer is equipped with a linear transfer function. The learning rate of the model is set as 0.001 and the neural unit number in the hidden layer is 30 and 5 respectively.

Sixty-one sets of data points have been tested after adapting the models. The load thickness ranges from 0.1mm to 10mm and the temperature ranges from -30℃ to 40℃. Surface status recognition and load thickness regression have been done at the same time in the models. The thickness of ice is labeled as a positive value and water is labeled as a negative value, with zero standing for a dry condition and in the status-recognition program, a thickness below 0.1mm is considered as a dry condition. The distribution of validation error and the test error is shown in Fig. 10, and validation curves without temperature compensation are also given in the figure. Fig. 10(c) shows the error distribution of the SVR model, and Fig. 10(d) shows the error distribution of the ANN model.

All these six groups of error values do not exceed their thickness values in the first and third quadrants of Fig. 10(c) and (d), and the error values of a dry condition never exceed 0.1mm, which means the accuracy of surface status recognition in these models is always 100%. Moreover, accuracy of the validation curves is better than the test curves in this experiment, since the train sets always contain data points of the same thickness as validation sets do. Load thicknesses in test sets were randomly chosen, and thus, they do not usually overlap with the train sets. The generalization ability of the models are tested in the reproducibility test experiment. Validation error in the SVR and ANN models is generally the minimum in the figure, and the validation error without temperature compensation is apparently larger than the one with temperature compensation. As for the test sets, error is the largest among the three groups. All the three kinds of error values in the figure turn out to increase with the growing of load thickness, which is consistent with the trend of the features in Fig. 9.

Table 3 Surface load thickness measurement accuracy of all tested methods

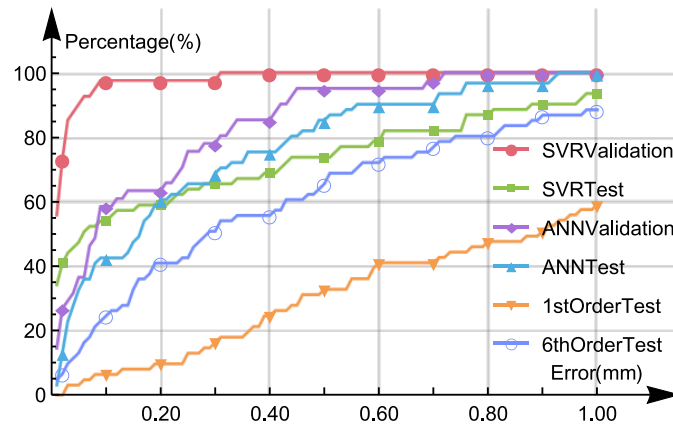| Method		Accuracy (1.00mm)
1st Order	Validation	70.97%
	Test	59.02%
6th Order	Validation	90.32%
	Test	88.52%
SVR	Validation	100.00%
	Test	93.44%
ANN	Validation	100.00%
	Test	100.00%

Fig. 11. Detailed error curves of the fitting curve methods, the SVR and the ANN models. The values on the percentage axis stand for the ratio of error values, which are less than the corresponding error values on the error axis.

Notably, most of the SVR model outputs tend to be lower than the ground truth, whereas the ANN model is more balanced, and the test error of the SVR model is much larger than that of the ANN model. Detailed error curves are shown in Fig. 11. The validation curve of the SVR model is nearly perfect, 96.7% of output has better accuracy of 0.10mm and 100.0% of output and has a better accuracy of 0.31mm. However, the test curve of the SVR model is the worst among all the error curves. It only reaches 73.6% and 93.4% at an error of 0.50mm and 1.00mm. This can be caused by a shortage of generalization ability or model overfitting. Fig. 10(a) shows that the error that affects the accuracy curve of the test is mainly with thick water. If the SVR model has been adapted too much, the error might be more balanced on the thickness axis, since the thickness of test sets is basically evenly distributed on the thickness axis. Thus, the generalization ability should be the main problem of the SVR model. The structure and parameters of this SVR model need further adjustment for better performance. On the other hand, the ANN model is more practical, and the validation curve of ANN model is close to the test curve, which means the generalization ability of ANN is better and the overfitting problem is acceptable in this model. All the output in the validation curve has better accuracy of 0.72mm and the test curve reaches 85.5% and 100.0% at the error of 0.50mm and 1.00mm. As the test accuracy is the most important indicator of model evaluation, the ANN model performed better than the SVR model in this experiment.

Compared with the fitting curve method, the machine-learning method shows superiority in measurement accuracy and stability. The error distribution of the ANN model is apparently better than that of the sixth order resonance frequency fitting curve and the test error is smaller when the ice film is thin, and it makes the sensor's reading more stable when measuring black ice. Table 3 shows the measurement accuracy of the surface load thickness of these four methods at the error of 1.00mm. The data suggest that the first order resonance frequency is not suitable for thickness calculation, whereas the ANN model is the best calibration tool among the four methods, and the SVR model is slightly better than the sixth order resonance frequency fitting curve. The test results of fitting curve methods are also shown in Fig. 11. The sixth order resonance frequency is far better than the first order resonance frequency, and the improvement of accuracy made by the former reaches 32.79% at 0.50mm and 29.51% at 1.00mm. The ANN test curve goes beyond the conventional method's test curve from 0.01mm to 1.00mm, and the accuracy improvement reaches 62.34% and 40.98% at 0.50mm and 1.00mm respectively.
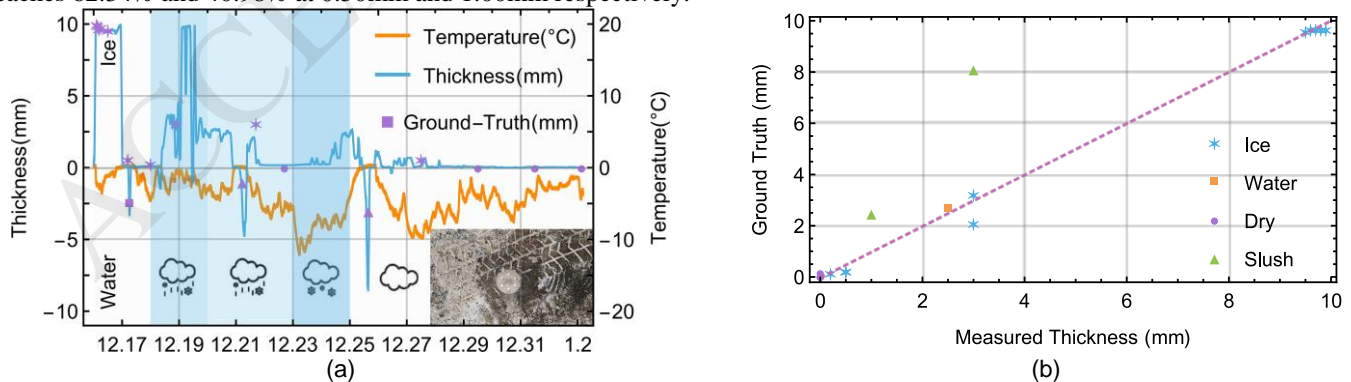

Fig. 12. (a) Result of an eighteen-day field test on the roads of the Norwegian University of Science and Technology. The picture of the installed sensor is shown in bottom right corner. The ground-truth data are shown in purple symbols, asterisk stands for ice, dot stands for dry, square stands for water and triangle stands for slush. The weather data are presented with symbols and blue regions, the deeper color means heavier snowing. (b) The measured film thickness and the ground truth obtained with micrometer.

The prototype of road status sensor was tested on the roads of Norwegian University of Science and Technology (NTNU,

Gjøvik) from 2016/12/16 to 2017/1/2. The sensor was embedded on a wheel track of a hill, where some cars and snow clearers would go through occasionally. It was installed in a hole and the cable lied in the trunking, epoxy resin was used to fill in the free space of the hole and trunking. The structure was so stable that no sign of affection from the internal road stress was found during the test.

The load thickness obtained by the ANN model and the temperature data are shown in Fig. 12. The positive values of load thickness stand for ice film thickness, and the negative ones stand for water film thickness. The sensor was covered with thick snow when the installation was completed. For several times the thickness of the ice film decreased sharply, it could be caused by ice removal and vehicle roller compaction.

As a matter of validation, ground-truth data collected during the test are plotted in the figure, different symbols are used to indicate the observed road surface status, asterisk stands for ice, dot stands for dry, square stands for water and triangle stands for slush. Moreover, weather data from the Norwegian Meteorological Institute are referred to, and the data suggest that there were freezing rain and snowfall on 19th, 21th, 22th, 24th with the precipitation of 2.6mm, 0.1mm, 0.4mm and 6.9mm respectively. The time of snowfall matches well with the ice thickness reading increasing time stage. Thus the weather data agree with the sensor's output to some extent.

On the other hand, when ice melted, the thickness of ice and water films don't match. This phenomenon seriously affects the reliability of the sensor reading. According to the record, the ground-truth data basically agree with ice film and dry surface measurement results, the maximum error is below 1.0mm. But the water film measurement results are higher than expected, the maximum error is about 5.5mm. And the recorded road status data show that it was the slush caused the error. Slush is a mixture of water, ice and wet snow. It exists when the earth temperature is around 0 centigrade degree, it can significantly increase the mass and damping of the vibration system, whereas it won't affect the equivalent bending modulus. As a result, slush can lead to change of amplitude frequency response and the features behave like heavy water status. This problem must be solved, potential method is to combine other kind of sensors with the piezoelectric sensor to achieve various statuses recognition and better measurement ability.

V. CONCLUSION

This work has gone one step further on the bases of Roy's and Li's studies, and places the piezoelectric sensor into a new application field. The road status sensor driven by the frequency scanning method has collected much information of the status on its surface. Finite element analysis helped study the characteristics of amplitude frequency response curve when different kinds of load were added. The features extraction simplified the data, and then artificial neural network calculated the road status and load thickness. As a result, the road status sensor and the artificial neural network achieve perfect surface status recognition and enough accurate measurement of ice and water film with a larger measurement range and stable readings, which have made progress compared with conventional fitting curve methods. This work extends the measurement limit of the road status sensor from about 1.4mm [10] to 10.0mm, but the absolute error is worse than some other sensors. This is mainly caused by the extension of measurement range and temperature drift, which have not been paid much attention in previous studies. The sensor has been tested on the road of Norwegian University of Science and Technology for eighteen days and performed well. This field test serves as a proof of concept that a piezoelectric sensor based on a machine-learning algorithm offers a new strategy to monitor road status. Once the road status sensor is connected to a geometric information system, it will make a contribution to the development of an intelligent transportation system, especially in cold regions.

On the other hand, although some progress was made in this study, there are also limitations. The road surface status is complicated than it is in the lab, for instance, slush and ice covered with snow are hard to measure with this sensor, so a multi-sensor based detector will be needed. Sensors based on optical principle and other technologies can be integrated with the piezoelectric sensor, and thereby more road status can be accurately recognized. From another perspective, the nine features extracted in this work are not sensitive to the increasing of load thickness when the load is more than 4mm, and some of them drift a great deal with temperature. Therefore, another future direction is to carry out better feature extraction from the multi-sensor detector. More importantly, the machine learning model significantly influences the accuracy of the measurement, so future iterations of different algorithms may, in fact, demonstrate even greater potency.

APPENDIX

A. Amplitude frequency response characteristic

As is shown in Fig. 1, the whole vibration system can be considered as an elastic thin plate with small deflections, because the thickness of the vibration system H is far less than 2/5 of the neutral strain plane's radius R and the maximum deflection w_{max} of any point in the neutral strain plane is much less than 1/5 of H. Thus, the elastic potential energy U of the vibration system can be expressed as

$$U = \frac{1}{2} \iiint_V (\sigma_\rho \varepsilon_\rho + \sigma_\theta \varepsilon_\theta + \sigma_z \varepsilon_z) dV, \qquad (A.1)$$

with σ being the stress and ε being the deformation of the infinitesimal. And the bending modulus D of the vibration system is obtained as

$$D = \frac{EH^3}{12(1-\mu^2)}, \tag{A.2}$$

where E and μ stands for the equivalent elastic modulus and Poisson's ratio of the vibration system respectively. Consider an arbitrary point M in the neutral strain plane, according to the geometric equation, generalized Hooke law and equilibrium equation. The elastic potential energy U in Eq. (A.1) can be transferred into

$$U = \frac{D}{2} \iint_S \left[\left(\frac{\partial^2 w}{\partial a^2}\right)^2 + \frac{2\mu}{a}\frac{\partial w}{\partial a}\frac{\partial^2 w}{\partial a^2} + \frac{1}{a^2}\left(\frac{\partial w}{\partial a}\right)^2 \right] a\,da\,d\theta$$
$$= \pi D \int_0^R \left[\left(\frac{\partial^2 w}{\partial a^2}\right)^2 + \frac{2\mu}{a}\frac{\partial w}{\partial a}\frac{\partial^2 w}{\partial a^2} + \frac{1}{a^2}\left(\frac{\partial w}{\partial a}\right)^2 \right] a\,da$$
$$\tag{A.3}$$

where w is the deflection of point M in normal direction and a is the distance between M and the origin. According to differential equations of elastic surfaces, the deflection function for elastic thin plate is obtained as

$$W = \frac{q_0 R^4}{64D}\left(1 - \frac{a^2}{R^2}\right)^2, \tag{A.4}$$

where q_0 is a function of surface traction. If the thin plate vibrates with angular frequency ω and mode $W(x,y)$ with t being time, consider the moment when thin plate passes the equilibrium position as initial time, then the instantaneous deflection function can be states as

$$w = W(x,y)sin\omega t. \tag{A.5}$$

Plugging the fixed boundary condition, Eq. (A.4) and Eq. (A.5) in Eq. (A.3), the maximum elastic potential energy U_{max} can be written as

$$U_{max} = \pi D \int_0^R \left[\left(\frac{\partial^2 W}{\partial a^2}\right)^2 + \frac{1}{a^2}\left(\frac{\partial W}{\partial a}\right)^2 \right] a\,da. \tag{A.6}$$

On the other hand, the kinetic energy theorem states that the kinetic energy of the vibration system can be expressed as

$$T = \frac{1}{2}\iint_S m\left(\frac{\partial w}{\partial t}\right)^2 dxdy, \tag{A.7}$$

with m representing equivalent mass per unit area. Plugging the fixed boundary condition and Eq. (A.5) in Eq. (A.7), the maximum kinetic energy T_{max} can be obtained by

$$T_{max} = \pi \omega^2 \int_0^R mW^2 a\,da. \tag{A.8}$$

According to the energy conservation principle, U_{max} should be equal to T_{max}, so combine Eq. (A.4), Eq. (A.6) and Eq. (A.8) together, and the nature angular frequency can be solved as

$$\omega_n = \sqrt{\frac{320D}{3R^4 m}} = \sqrt{\frac{80EH^2}{9R^4(1-\mu^2)\rho}}, \tag{A.9}$$

where ρ stands for the equivalent density of the vibration system, and the resonance frequency f_r is obtained as

$$f_r = \frac{\omega_n}{2\pi} = \sqrt{\frac{20EH^2}{9\pi^2 R^4(1-\mu^2)\rho}}. \tag{A.10}$$

Based on the free vibration system with one degree of freedom, the amplitude frequency response function can be stated as

$$A(\omega) = \frac{1}{\sqrt{\left(1-\left(\frac{\omega}{\omega_n}\right)^2\right)^2 + \left(2\xi\frac{\omega}{\omega_n}\right)^2}}, \tag{A.11}$$

with ξ being the damping coefficient. So the amplitude frequency response curve of the first order mode vibration can be plotted.

B. Equivalent bending modulus model

As is shown in Fig. 1, ignoring the adhesion layer for its low thickness, the piezoelectric sensor is equivalent to a combination of two rigid layers, a piezoceramic disc layer with radius R, thickness h_p, Young's modulus E_p, density ρ_p, Poisson's ratio μ_p and an alloy plate layer with radius R, thickness h_a, Young's modulus E_a, density ρ_a, Poisson's ratio μ_a. From Eq. (A.9) and Eq. (A.11), it can be inferred that the amplitude frequency response is only related to the five parameters above and the damping coefficient of the system ξ. Thus, if the two rigid layers are considered as one circular disc transducer, an equivalent bending modulus model can be built. Furthermore, if an ice film or water film is deposited on the upper surface of the alloy plate, the equivalent model can be expanded, as is shown in Fig. B.1. The load's parameters are radius R, thickness h_l, Young's modulus E_l, density ρ_l, Poisson's ratio μ_l.
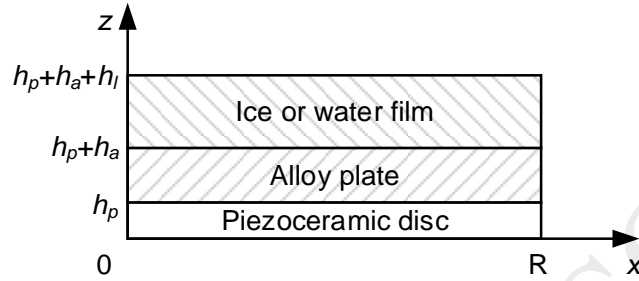

Fig. B.1 A schematic view of the vibration system with ice or water film on the upper surface of the alloy plate. The thickness of the load film is stated as h_l.

To apply Eq. (A.9) to this equivalent bending modulus model, some equivalent calculation is necessary. To begin with, equivalent mass per unit area m_{eqi} can be expressed as

$$m_{eqi} = \rho_p h_p + \rho_a h_a + \rho_l h_l, \quad (B.1)$$

and the radius of the circular disc can be seen as R. Then according to Eq. (A.2), the equivalent bending modulus D_{eqi} is related to thickness, equivalent elastic modulus and Poisson's ratio. This can be obtained by integral operation,

$$D_{eqi} = \int_0^{h_p} \frac{E_p(z - z_x)^2}{1 - \mu_p^2} dz + \int_{h_p}^{h_p+h_a} \frac{E_a(z - z_x)^2}{1 - \mu_a^2} dz$$
$$+ \int_{h_p+h_a}^{h_p+h_a+h_l} \frac{E_l(z - z_x)^2}{1 - \mu_l^2} dz$$
$$(B.2)$$

where z_x is the position of the neutral strain plane on the z axis. In accordance with the definition of neutral strain plane, the bending stress on this surface should be zero, so z_x can be obtained by solving

$$0 = \int_0^{h_p} \frac{E_p(z - z_x)}{r(1 - \mu_p^2)} dz + \int_{h_p}^{h_p+h_a} \frac{E_a(z - z_x)}{r(1 - \mu_a^2)} dz$$
$$+ \int_{h_p+h_a}^{h_p+h_a+h_l} \frac{E_l(z - z_x)}{r(1 - \mu_l^2)} dz$$
$$(B.3)$$

where r stands for the radius of curvature. For brevity, the Poisson's ratio expression can be contained in the Young's modulus expression, so D_{eqi} can be expressed as,

$$D_{eqi} = \int_0^{h_p} E_p'(z - z_x)^2 dz + \int_{h_p}^{h_p+h_a} E_a'(z - z_x)^2 dz$$
$$+ \int_{h_p+h_a}^{h_p+h_a+h_l} E_l'(z - z_x)^2 dz$$
$$(B.4)$$

thus z_x can be written as,

$$z_x = \frac{E_p' h_p^2 + E_a' h_a^2 + E_l' h_l^2 + 2E_a' h_p h_a + 2E_l' h_p h_l + 2E_l' h_l h_a}{2(E_p' h_p + E_a' h_a + E_l' h_l)}, \quad (B.5)$$

combine Eq. (B.2) and Eq. (B.5) together, D_{eqi} can be calculated.

$$
\begin{aligned}
D_{eqi} = [&E'_p E'_a h_p h_a (4h_p^2 + 4h_a^2 + 6h_p h_a) \\
&+ E'_p E'_l h_p h_l (4h_p^2 + 4h_l^2 + 6h_p h_l) \\
&+ E'_a E'_l h_a h_l (4h_a^2 + 4h_l^2 + 6h_a h_l) \\
&+ 12 E'_p E'_l h_p h_a h_l (h_p + h_a + h_l) \\
&+ E'^2_l h_l^4 + E'^2_a h_a^4 + E_p^2 h_p^4] \\
&/ 12 (E'_l h_l + E'_a h_a + E'_p h_p).
\end{aligned}
$$

(B.6)

Finally, ω_n and $A(\omega)$ can be numerically solved by plugging D_{eqi} into Eq. (A.9) and Eq. (A.11).

Acknowledgements

References

[1]   A. Klein-Paste and J. Wåhlin, "Wet pavement anti-icing — A physical mechanism," *Cold Reg. Sci. Tech.*, vol. 96, pp. 1-7, 2013. https://doi.org/10.1016/j.coldregions.2013.09.002
[2]   K. C. Dey, A. Mishra and M. Chowdhury, "Potential of Intelligent Transportation Systems in Mitigating Adverse Weather Impacts on Road Mobility: A Review," *IEEE Trans. Intell. Transp. Syst.*, vol. 16, (3), pp. 1107-1119, 2015. https://doi.org/10.1109/TITS.2014.2371455
[3]   L. Hajibabai and Y. Ouyang, "Dynamic Snow Plow Fleet Management Under Uncertain Demand and Service Disruption," *IEEE Trans. Intell. Transp. Syst.*, vol. 17, (9), pp. 2574-2582, 2016. https://doi.org/10.1109/TITS.2016.2520918
[4]   M. Yamada, K. Ueda, I. Horiba and N. Sugie, "Discrimination of the road condition toward understanding of vehicle driving environments," *IEEE Trans. Intell. Transp. Syst.*, vol. 2, (1), pp. 26-31, 2001. https://doi.org/10.1109/6979.911083
[5]   C. Q. Gómez Muñoz, F. P. García Márquez and J. M. Sánchez Tomás, "Ice detection using thermal infrared radiometry on wind turbine blades," *Measurement*, vol. 93, pp. 157-163, 2016. https://doi.org/10.1016/j.measurement.2016.06.064
[6]   L. Colace, F. Santoni and G. Assanto, "A near-infrared optoelectronic approach to detection of road conditions," *Opt. Lasers Eng.*, vol. 51, (5), pp. 633-636, 2013. https://doi.org/10.1016/j.optlaseng.2013.01.003
[7]   X. Gong and S. Bansmer, "Laser scanning applied for ice shape measurements," *Cold Reg. Sci. Tech.*, vol. 115, pp. 64-76, 2015. https://doi.org/10.1016/j.coldregions.2015.03.010
[8]   A. A. Ikiades, G. Howard, D. J. Armstrong, M. Konstantaki, and S. Crossley, "Measurement of optical diffusion properties of ice for direct detection ice accretion sensors," *Sens. Actuator A-Phys.*, vol. 140, (1), pp. 24-31, 2007. https://doi.org/10.1016/j.sna.2007.05.036
[9]   J. Ge, L. Ye, and J. Zou. "A novel fiber-optic ice sensor capable of identifying ice type accurately," *Sens. Actuator A-Phys.*, vol. 175, (4), pp. 35-42, 2012. https://doi.org/10.1016/j.sna.2011.12.016
[10]   X. Li, W. Y. Shih, J. Vartuli, D. L. Milius, R. Prud'homme, I. A. Aksay and W. H. Shih, "Detection of water-ice transition using a lead zirconate titanate/brass transducer," *J. Appl. Phys.*, vol. 92, (1), pp. 106-111, 2002. https://doi.org/10.1063/1.1481191
[11]   S. Roy, A. Izad, R. G. DeAnna and M. Mehregany , "Smart ice detection systems based on resonant piezoelectric transducers," *Sens. Actuator A-Phys.*, vol. 69, (3), pp. 243-250, 1998. https://doi.org/10.1016/S0924-4247(98)00101-0
[12]   T. Bai, C. L. Zhu, Q. Li and C. X. Zhu, "Study of Bimorph Piezoelectric Cantilever Structure Used on Icing Detection," *Acta Aeronautica Et Astronautica Sinica*, vol. 34, (5), pp. 1073-1082, 2013. https://doi.org/10.7527/S1000-6893.2013.0196
[13]   X. Zhao and J. L. Rose, "Ultrasonic guided wave tomography for ice detection,"*Ultrasonics*, vol. 67, pp. 212-219, 2016. https://doi.org/10.1016/j.ultras.2015.12.005
[14]   Dan Fuleki, Zhigang Sun, Jason (Kuo-Ting) Wu, and Grael Miller. "Development of a Non-Intrusive Ultrasound Ice Accretion Sensor to Detect and Quantify Ice Accretion Severity", presented at *the 9th AIAA Atmospheric and Space Environments Conference*, AIAA AVIATION Forum, Denver, USA, Jan. 5-9, 2017 https://doi.org/10.2514/6.2017-4247
[15]   C. Du, Q. Wang, X. Liu, Y. Zhao, X. Deng and L. Cui, "Research and Application of Ice Thickness and Snow Depth Automatic Monitoring System," *IEEE Trans. Instrum. Meas.,* vol. 66, (2), pp. 325-331, 2017. https://doi.org/10.1109/TIM.2016.2636518
[16]   H. Tabatabai and M. Aljuboori, "A Novel Concrete-Based Sensor for Detection of Ice and Water on Roads and Bridges," *Sensors*, vol. 17, (12), pp. 2912, 2017. https://doi.org/10.3390/s17122912
[17]   K. P. Owusu, D. C. S. Kuhn and E. L. Bibeau, "Capacitive probe for ice detection and accretion rate measurement: Proof of concept," *Renew. Energy*, vol. 50, pp. 196-205, 2013. https://doi.org/10.1016/j.renene.2012.06.003
[18]   A. Troiano, E. Pasero and L. Mesin, "New System for Detecting Road Ice Formation," *IEEE Trans. Instrum. Meas.*, vol. 60, (3), pp. 1091-1101, 2011. https://doi.org/10.1109/TIM.2010.2064910
[19]   M. Zivanovic, "Temperature-Compensated Microstrip Antenna for Ice Measurement and Wireless Sensor Network." M.S. thesis, Dept. Electron. Eng., Montreal Univ., Montreal, Canada, 2018.
[20]   V. V. Viikari, T. Varpula and M. Kantanen, "Road-Condition Recognition Using 24-GHz Automotive Radar," *IEEE Trans. Intell. Transp. Syst.*, vol. 10, (4), pp. 639-648, 2009. https://doi.org/10.1109/TITS.2009.2026307

Biographies

Kang Gui received the B.S. degree in measurement and control technology and instrumentations from Huazhong University of Science and Technology, Wuhan, Hubei, China, in 2013, where he is currently pursuing the Ph.D. degree. His research interests are in road status sensors, multi-sensor data fusion, deicing system and road weather information system.

Lin Ye was born in Wuhan, Hubei, China in 1960. He received the B.S. and M.S. degrees from Huazhong University of Science and Technology, Wuhan, Hubei, China, in 1982 and 1988, respectively, both in measurement technology and instrumentations. From 1992 to 1993, he was a visiting scholar at Department of Automation, Moscow Institute of Power Engineering, Moscow, Russia. And from 1998 to 1999, he was a visiting scholar at Department of Aeronautics and Astronautics, Washington University, Washington, USA. From 2004, he has been a Professor with the Department of Automation, Huazhong University of Science and Technology. His current research area covers ice sensors, aircraft deicing system, in-situ emissivity measurement and non-contact temperature measurement.

Junfeng Ge received the B.S. degree in measurement and control technology and instrumentations from Huazhong University of Science and Technology, Wuhan, Hubei, China, in 2003. He received the M.S. and Ph.D. degrees in control science and engineering from Tsinghua University, Beijing, China, in 2005 and 2009, respectively. He is currently an Associate Professor with the Department of Automation, Huazhong University of Science and Technology. His research interests include ice detection, pattern recognition and instrumentation.

Lizhen Huang received the B.S. degree in civil engineering from Chongqing Jiatong University of Science, Chongqing, China, in 2000 and 2003, respectively. She received the Ph.D. degrees in management science from Tongji University, Shanghai, China, in 2006. She is currently an Associate Professor with the Department of manufacturing and civil engineering, NTNU, Norwegian University of Science and Technology. Her research interests include sustainable built environment with digitalization.